PHYSICAL REVIEW B VOLUME 27, NUMBER 6 15 MARCH 1983

# Transport in lateral surface superlattices

R. K. Reich, R. O. Grondin, and D. K. Ferry
*Department of Electrical Engineering, Colorado State University, Fort Collins, Colorado 80523*
(Received 30 August 1982; revised manuscript received 19 November 1982)

A numerical Monte Carlo simulation is carried out to find the velocity and energy as a function of the electric field for a surface superlattice structure. The energy is found to saturate at the half-filled-band energy, while the velocity displays a negative differential conductivity. The scattering rates included in the Monte Carlo routine have Van Hove singularities arising from the electron density of states. This singularity is removed by including a self-energy correction to the electron Green's function. The simulations indicate that the negative differential conductivity is due to Bloch oscillations of the electrons.

## I. INTRODUCTION

The present understanding of device physics has advanced to the point where quantum interactions can be used to develop novel device concepts. Not only must quantum effects be taken into account when characterizing next-generation devices in tight arrays or structures such as metal-oxide-semiconductor (MOS) or charge-coupled device (CCD) arrays, they can lead to new conceptual phenomena. Individual devices (or structures) begin to interact with their surrounding environment when the critical spacing of such systems becomes comparable with the de Broglie wavelength in that system. This preempts the device from being treated as an isolated entity and thereby makes it necessary to reasonably account for environmental interactions. The work reported here investigates the quantum interactions in a structure which is described as a lateral surface superlattice (LSSL).

In particular, the velocity-electric field curves of the lateral surface superlattice are calculated using a Monte Carlo simulation. The curves from the simulation show a definite region of negative differential mobility. This is found to be caused by Bloch oscillations occurring from quantum interactions within the LSSL.

Kroemer[1] first proposed a microwave amplifier using the quantum-derived sinusoidal bands. He suggested that the electrons would exhibit a negative mass if they could be excited to the top of the band. This would cause a reduction in the velocity for an increase of the electric field and thus produce negative differential conductivity. Such a condition could be used to produce amplification. In order for this to actually happen, the bands must be sufficiently narrow that the electrons can be accelerated to the top of the band before they are scattered by phonons or some other mechanism. Unfortunately, in all semiconductors studied thus far the combination of bandwidth and electron-phonon scattering prohibits this process from occurring. If one could obtain a narrower bandwidth, the effects could be observed. Such narrowing can be achieved by the creation of a miniband structure inside the normal conduction band.

Peierls[2] discussed a general distortional instability that would introduce minigaps in the conduction-electron spectrum. This distortion superimposes a larger periodic potential upon the already existing potential from the lattice of atoms. The minigaps (and minibands) produce smaller dispersive energy ranges. Although Peierls was trying to explain the complicated shape of energy for electrons in metals and alloys, later methods suggested that the superpotential could be obtained by a superlattice, which would yield much the same results. Others[3–5] have developed the concept of charge-density waves which can create a superlattice potential with or without an applied external force. The charge-density waves are the result of a stable charge distortion, as suggested by Peierls, and modify the physical properties of the medium. In a self-consistent fashion, the zero of the dielectric response are responsible for a spontaneous charge instability creating a charge-density wave without the presence of an externally applied field.

Esaki and Tsu[6] developed the current interpretation of one-dimensional layered superlattices where, in the most common form, molecular-beam epitaxy is used to lay down, for example, alternate layers of GaAs and GaAlAs. The superlattice is obtained by periodic variation of an alloy composition or of impurity density introduced during epitaxial growth.[7] In this way, a generic semiconductor can be produced with not only the physical properties of the

 

host semiconductor, but with properties that also depend upon the structure of the superlattice. This allows the physical characteristics of such a system to be modified on demand by adjusting the critical spacing of layered material. This critical spacing (as compared to de Broglie wavelength) is the control parameter for the width of the energy bands and thus the electronic properties of the superlattice.

The energy dispersion in a superlattice band, such as that of Esaki and Tsu, is sufficiently narrow for an electric field to accelerate an electron to the top of the band. The problem Kroemer experienced, in which the energy dispersion is too broad, has now been overcome through the development of the superlattice, and the generic superlattice structure. However, there has not yet evolved definitive evidence indicating negative differential mobility (NDM) in the velocity-field curves. A possible explanation[8] for the lack of observation of NDM could be that the electrons in the quantized dimension (sinusoidal energy spectrum) are able to be scattered to an intermediate energy level in another subband since the other two dimensions remain nearly free in the effective-mass approximation. Thus the subbands actually overlap in the transverse dimension. Since these intermediate levels are in the gap of the quantized dimension, they therefore allow higher subbands to be populated. Electrons will be scattered to intermediate states before they can ever reach the edge of the reduced Brillouin zone. Although strong NDM may not be obtained, a resonant structure for the current, as a function of the field, could still develop.[9]

A lateral surface superlattice has three-dimensional quantization, as opposed to the conventional one-dimensional superlattice. Thus there are gaps in the energy spectrum in all three dimensions simultaneously, in contrast to the latter. The absence of intermediate energy levels provides for the possible existence of NDM in the velocity-field curves at relatively moderate fields. Since the electric field necessary to produce NDM is comparatively moderate, electrons cannot be excited to higher subbands through intermediate states within the same cell nor can they tunnel to higher subbands in neighboring cells. Bate[10] proposed such a structure, which formally is similar to a charge-coupled-device array. Although technology has not yet produced the required device density for the surface superlattice to be formed, it is within research limits of electron and ion-beam lithography for such a structure to be made. Another type of lateral surface superlattice is that on a tilted surface of Si [small tilt away from the (100) surface],[4] which was used to explain the valley splitting observed in Shubnikov—de Haas measurements of inversion layers at low temperatures. These experiments suggest that there are minigaps at the Si-$SiO_2$ interface which arise due to a surface superlattice.[4]

In this paper, the details of a theoretical Monte Carlo calculation for the velocity and energy are presented for a LSSL. A description of the scattering rates with Van Hove singularity corrections for the sinusoidal bands used in the Monte Carlo routine and the results of the Monte Carlo simulation are given. The simulation shows evidence of Bloch oscillations as the cause of negative differential mobility as will be apparent from the velocity-autocorrelation function. The distribution function is also obtained from the Monte Carlo simulation and again seems to indicate that Bloch oscillations are the cause of the NDM.

## II. THE MODEL

The specific model developed here is composed of cylinders of GaAs imbedded in a very thin epilayer of GaAlAs. The GaAs cylinders are arranged in a two-dimensional square-lattice array within the epilayer. The radius of the cylinders is taken to be 37.5 Å, while the spacing between cylinder centers is 100 Å. The system is considered to be operated at room temperature, so that the mass of both GaAs and GaAlAs (taken to be a direct band-gap material) may be taken as $0.068m_0$,[11] where $m_0$ is the free-electron mass. The form of the LSSL, as described above, is shown in Fig. 1.

The potential energy of the model is developed from the structural layout of the superlattice described in the preceding paragraph. The thin epilayer confines the electrons to a surface as a quasi-two-dimensional system.[12] The electron, in the direction perpendicular to the surface, therefore experiences infinite potential barriers at the boundaries of the epilayer. These potential barriers allow only widely-spaced, discrete energies. Indeed, for electron transport, one need consider just the other two dimensions, neglecting this third dimension. The

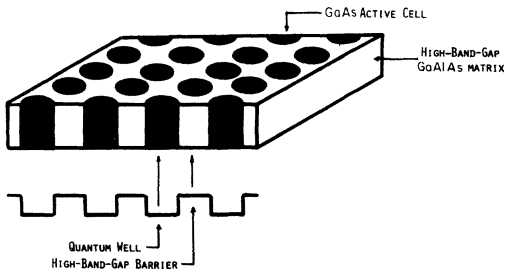


FIG. 1. Picture of the LSSL model for the calculation of energy dispersion. The cylinders of GaAs in GaAlAs produce the potential variation.

difference between the conduction-band energy of GaAs and GaAlAs generates cylindrical potential wells in the square-lattice array in the surface layer. This is necessary for the superlattice. The composition of GaAlAs alloy is adjusted so that the band edge is approximately 0.5 eV above the GaAs conduction-band edge for an Al concentration of 0.4 in $Ga_{1-x}Al_xAs$ (Ref. 13) at room temperature.

It should be noted that the model developed here is generic in form. The different parameters, including layout and material, can be changed while still retaining the superlattice nature of the structure. This allows the LSSL model to be applied to MOS structures where the system dimensions approach that of the de Broglie wavelength and the fields are very similar to that of the LSSL. In this way, possible coherent quantum effects can be studied to investigate the influence in such high-density very-large-scale integration (VLSI) structures.

The energy dispersion for the given physical parameters of this generic model has been calculated previously.[12] Two approaches were evaluated to ensure the validity of the results. The first involved a linear combination of atomic orbitals (LCAO) technique in which Bessel functions, evolving from the cylindrical wells, were used as the atomic orbitals. The second approach gave rise to a Mathieu equation, the solutions of which are Bloch functions. The two methods of calculation were in good agreement for the same set of parameters. The details of the approaches that lead to the energy spectrum will not be given here, but only the resulting energy equation, which is[14]

$$E=\epsilon-(\epsilon/2)[\cos(k_xD)+\cos(k_yD)]\ , \tag{1}$$

where $\epsilon=0.05$ eV is the half-filled-band energy and $D=100$ Å is the spacing between potential wells for the parameters selected here. The general form of this expression has also been found for one-dimensional layered superlattices,[9] where the bands are sinusoidal in only one dimension. The above expression is used in the Monte Carlo simulation below to obtain the velocity-field curves.

## III. SCATTERING RATES

The scattering rates for the GaAs-GaAlAs LSSL are developed in this section starting from the transition-matrix element corresponding to the particular scattering. For GaAs and GaAlAs, the dominant scatterers at room temperature (which is the temperature assumed throughout) are acoustic and polar-optical phonons. A Van Hove[15] singularity appears in the evaluation of the scattering rate and is resolved near the end of the present section by a smoothing of the usual Green's-function energy-conserving $\delta$ function. This leads to replacement of the latter by a Lorentzian curve. Since the energy spectrum is of complex nature, the total scattering rate from a state $\vec{K}$ can only be evaluated numerically. The matrix elements are calculated as a function of $\vec{K}$ and $\vec{K}'$, at which time the $\vec{K}'$ is numerically integrated. Graphs of the scattering rates are the final output of this approach, and show only an energy dependence as expected.

Because of the discrete energy levels of the perpendicular dimension in the LSSL, most of the calculation involves only two dimensions. The third dimension in most cases is normalized out of the problem, allowing a two-dimensional analysis to be used.

Fermi's golden rule[16] is used as the initial expression for the transition probability in the electron-phonon interaction. Therefore, it is assumed that the interaction is turned on adiabatically and the collisions are instantaneous in time. The energy-conserving term in the transition probability can then be interpreted as a $\delta$ function. The general analytical expression for the transition probability is thereby given for the acoustic deformation-potential scattering rate as[16,17]

$$\lambda(\vec{K})=\int dV_{K'}S(\vec{K},\vec{K}')$$
$$=\frac{4\pi}{\hbar}\frac{A}{4\pi^2}\int dV_{K'}\frac{\hbar^2E_1^2q^2}{2MN\omega_q}\frac{k_BT}{\hbar\omega_q}\delta(E_K-E_{K'})\ , \tag{2}$$

where it has been assumed that $\hbar\omega_q \ll k_BT_j$ so that $\exp(\hbar\omega_q/k_BT)\cong 1$ and

$$n_q\cong n_q+1\cong k_BT/\hbar\omega_q\ .$$

This is just the equipartion limit. The usual sum over wave vectors has been converted to an integral (in two dimensions) through

$$\sum_{K'}\rightarrow\frac{A}{4\pi^2}\int dV_{K'}\ .$$

Using the linear relation for the phonon-dispersion curve, $\omega_q=uq$ ($u$ is the velocity of sound), (2) becomes

$$\lambda(\vec{K})=\frac{2\pi E_1^2k_BT}{NM\hbar u^2}\frac{A}{4\pi^2}\int dV_{K'}\delta(E_K-E_{K'})\ , \tag{3}$$

$dV_K$ is an integration over two-dimensional $\vec{K}$ space where the energy is sinusoidal, so that the argument in the $\delta$ function can be written in Cartesian coordinates as

$$E_K=\epsilon-(\epsilon/2)[\cos(K_x'D)+\cos(K_y'D)]\ , \tag{4}$$

and

$$dV_{K'}=dK_x'\,dK_y' .$$

Integrating the $\delta$ function of (3) with respect to $K_y'$, the scattering rate transforms to

$$\lambda(\vec{K})=\frac{2\pi E_1^2 k_B T}{NM\hbar u^2}\frac{A}{4\pi^2}\left[\frac{2}{D\epsilon}\right]\times\int dK_x'\left[1-\left[\frac{2(\epsilon-E_K)}{\epsilon}-\cos(K_x'D)\right]\right]^{-1/2} . \tag{5}$$

The scattering rate can also be integrated over $K_x'$, but this does not further the understanding of the process. In fact, when the scattering rate for the polar-optical phonons is determined it will be found that this integral cannot be integrated. The integration over $K_x'$ leads to elliptic integrals of complicated form, so that it takes a very detailed analysis to extract any physical phenomena.

The numerical integration of (5) by a simple trapezoidal rule is shown in Fig. 2. Note that the scattering rate is symmetric about the half-filled-band energy as it should be for a sinusoidal band and also is singular at this same point. The singularity is the result of the saddle point of the two-dimensional density of states for sinusoidal bands and is better known as a Van Hove singularity. The singularity is removed below with the use of a phonon self-energy correction in the Green's function. The Van Hove singularity at the saddle point in the density of states is the point where the denominator of the integrand in (5) vanishes.

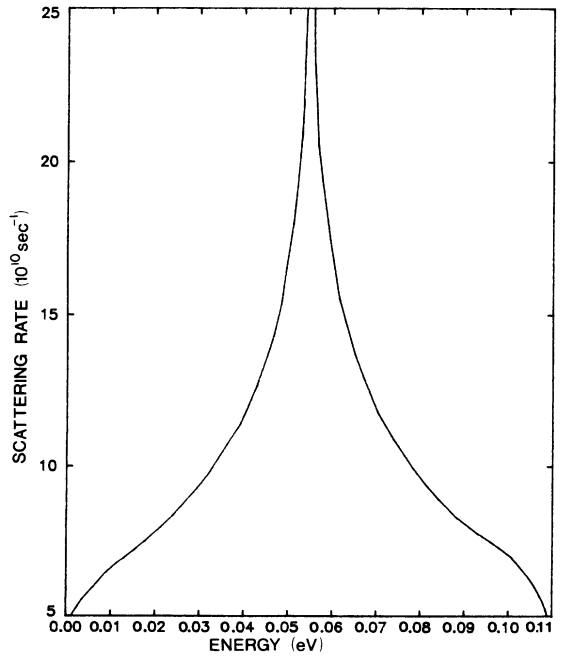


FIG. 2. Scattering rate vs energy for acoustic phonons for the LSSL. A Van Hove singularity occurs at half-filled-band energy.

The singularity is handled by the use of a phonon self-energy correction that is found to be important only in a small region around the singularity. Otherwise, the self-energy correction is of insignificant value and can be ignored in the Green's function. The electron Green's function, without the phonon correction, in general is[18]

$$G(t,t')=e^{i\omega(t-t')} ,$$

with

$$\hbar\omega=E_K-E_{K'} .$$

The Fourier transform of the causal component of the Green's function, with respect to time, leads to the replacement of the usual $\delta$ function for the matrix element in the "golden-rule" approximation by a Lorentzian of the form

$$\delta(E_K-E_{K'}\pm\hbar\omega_q)\rightarrow\frac{1}{2\pi}\frac{1}{(E_K-E_{K'}\pm\hbar\omega_q)^2+\lambda^2(E)} , \tag{6}$$

with

$$\lambda(E)=\frac{\hbar}{\tau(E)} ,$$

where in the above $\hbar\omega_q$ has been included for later use where the polar-optical phonons are evaluated. The above is just a statement of the finite-time duration of an electron in a specified energy state.

The scattering rate can now be written as a function of energy and has an integral structure after (6) is substituted into (3) for the $\delta$ function. This replacement gives

$$\lambda(E_K)=A\int\int\frac{\lambda(E_K)}{\eta^2(K_x,K_y)+\lambda^2(E_K)}dK_x dK_y , \tag{7}$$

where

$$\eta(K_x,K_y)=E_k-\{\epsilon-(\epsilon/2)\times[\cos(K_xD)+\cos(K_yD)]\} ,$$

$$C=\frac{E_1^2 k_B TA}{\hbar Nu^2 2\pi} .$$

Since the present concern is in computing an upper limit to the scattering rate, expression (7) can be estimated in the vicinity of the half-filled-band energy.

In the region of the singularity, the relation

$\eta(E) \ll \Gamma$ enables $\sin(K_x D)$ to be approximated at its maximum value of one without affecting the result. This allows the scattering rate to be expressed as

$$\lambda(E)=4C\int_0^{\pi/D}\sqrt{2}dK_x\int\frac{\lambda(E)}{(\epsilon_1\delta)^2+\lambda^2(E)}d\delta$$

$$=4C\frac{\sqrt{2}\pi^2}{D^2}\sqrt{2}\int\frac{\lambda(E)}{(\epsilon_1\delta)^2+\lambda^2(E)}d\delta\,. \quad (8)$$

The limits on the remaining integral can be taken to infinity since the integral has significant value only in the region of the half-filled-band energy. The integral is now evaluated, and finally the algebraic equation can be solved for the upper value of the scattering rate for acoustic phonons

$$\lambda_m=9.5\times10^{+11} \quad (9)$$

in units of $\sec^{-1}$. A maximum value is obtained which restricts all other values of the scattering rate. A more complex and less instructive procedure would find the detailed smoothing of the curve due to the self-energy correction, but is not done in this work as the upper limit in (8) is reached only near $E\cong\epsilon$ and lies well above the data of Fig. 2.

A similar analysis for the evaluation of the polar-optical phonons scattering rates can be applied. The only differences occur in the wave-vector dependence in the matrix elements and in the energy-dependent $\delta$ function which now also contains the phonon energy.

The scattering rate can be calculated with the substitution of the appropriate matrix element into (2), which leads to the relation

$$\lambda(\vec{K})=\frac{2\pi}{\hbar}\left[\frac{\hbar e^2}{2\gamma V\omega_0}\right]\int\int dK_x'dK_y'\frac{1}{\vec{q}^2}[n_q\delta(\vec{K}+\vec{q}-\vec{K}')\delta(E_{K'}-E_K-\hbar\omega_q)$$
$$+(n_q+1)\delta(\vec{K}-\vec{q}-\vec{K}')\delta(E_K-E_{K'}-\hbar\omega_q)]\,. \quad (10)$$

The summations over $\vec{K}'$ are once more transformed into integrals. There is an implicit sum over all phonon wave vectors, which enables the $\delta$ functions in wave vectors to be integrated. If this is done, (10) simplifies to

$$\lambda(\vec{K})=\frac{2\pi}{\hbar}\left[\frac{\hbar}{2\gamma}\frac{e^2}{Vw_0}\right]\frac{A}{4\pi^2}\int\int dq_x dq_y\left[\frac{1}{q_x^2+q_y^2}\right][n_q\delta(E_{|\vec{K}+\vec{q}|}-E_K-\hbar\omega_q)$$
$$+(n_q+1)\delta(E_K-E_{|\vec{K}-\vec{q}|}-\hbar\omega_q)]\,. \quad (11)$$

Substituting the functional relation for the energy ($E$) in terms of the wave vector ($\vec{K}$) and integrating over the phonon wave vector $q_y$, one obtains the expression

$$\lambda(\vec{K})=\left[\frac{e^2}{\gamma V\omega_0}\right]\frac{A}{4\pi}\left[n_q\int dq_x\frac{D\epsilon}{2}\left\{(q_x-K_x)^2+\left[\frac{1}{D}\cos^{-1}\left[\frac{2(\epsilon-E_I)}{\epsilon}-\cos(q_xD)-K_y\right]\right]^2\right\}^{-1}\right.$$
$$\times\left[1-\left[\frac{2(\epsilon-E_I)}{\epsilon}-\cos(q_xD)\right]^2\right]^{-1/2}$$
$$+(n_q+1)\int dq_x\frac{D\epsilon_1}{2}\left\{(q_x+K_x)^2+\left[\frac{1}{D}\cos^{-1}\left[\frac{2(\epsilon-E_I')}{\epsilon}-\cos(q_xD)\right]+K_y\right]^2\right\}^{-1}$$
$$\left.\times\left[1-\left[\frac{2(\epsilon-E_I')}{\epsilon}-\cos(q_xD)\right]^2\right]^{-1/2}\right], \quad (12)$$

with the limits

$$\cos(q_xD)<3-\frac{2E_I^{(\prime)}}{G_1}\,,$$
$$\cos(q_xD)>1-\frac{2E_I^{(\prime)}}{\epsilon_1}\,, \quad (13)$$

where

$$E_I=E_K-\hbar\omega_0\,,$$
$$E_I'=E_K+\hbar\omega_0\,.$$

Here $E_I$ ($E_I'$) indicates the energy $E_I$ ($E_I'$) satisfying

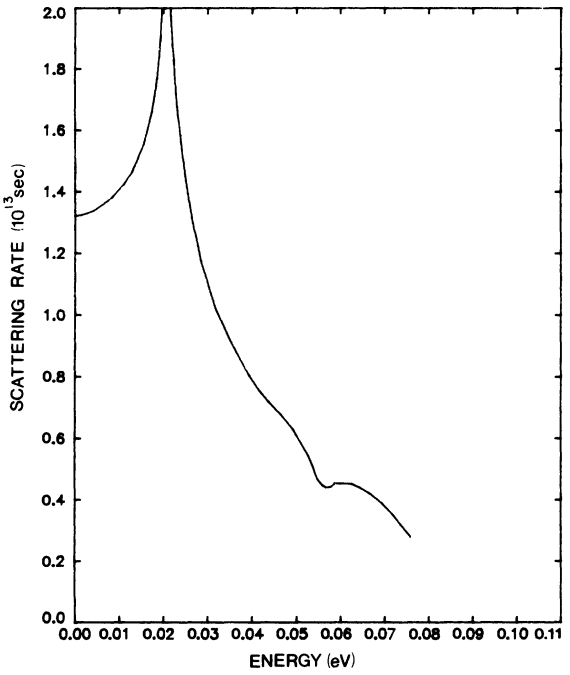


FIG. 3. Scattering rate vs energy for polar-optical phonon absorption for the LSSL. A Van Hove singularity occurs at half-filled-band energy minus phonon energy ($\hbar\omega_0=0.036$).

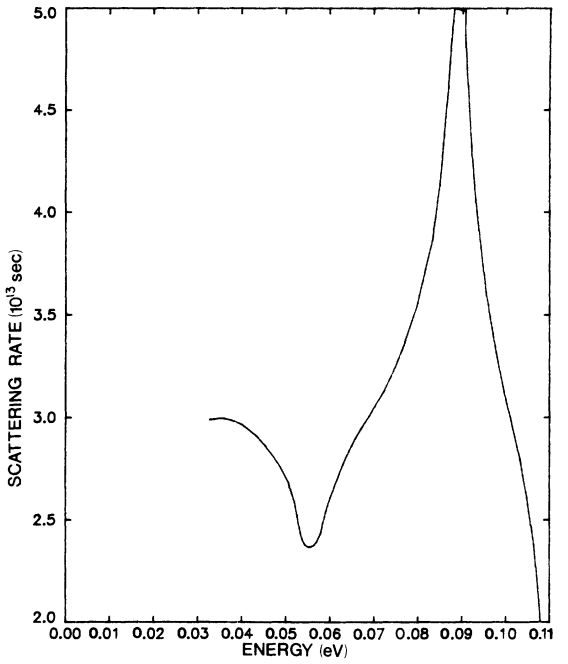


FIG. 4. Scattering rate vs energy for polar-optical phonon emission for the LSSL. Van Hove singularity occurs at half-filled-band energy plus phonon energy ($\hbar\omega_0=0.036$).

the first (second) integral.

The scattering rate (12) is almost unmanageable. The only reasonable manner in which to continue the analysis is to convert to numerical techniques. A trapezoidal integration[19] of (12) allows a graphic representation of the scattering rate. The first integral (for absorption) and the second (for emission) generate the curves shown in Figs. 3 and 4. The curve for absorption has a singularity at half-filled-band minus the phonon energy. This is just where it is expected, since the electron density of states to which an electron can be scattered is infinite at this point. Likewise, the emission term has a singularity at the half-filled-band plus phonon energy for the same density-of-states argument.

The scattering rate curves, in this case, should not be completely symmetric because of the square of the inverse wave vector in the integral [Eq. (12)]. The wave-vector dependence, it will be remembered, was obtained from the matrix element. In the Monte Carlo simulation, this inverse $q$ dependence produces Shockley streaming. The emission rate is higher than the absorption rate due to the phonon occupation factor.

The approach used for limiting the scattering rates for polar-optical phonons is similar to that used above for acoustic phonons. However, an exception arises due to the inverse-squared wave-vector dependence and the inclusion of phonon energy.

Following the same approach as given above for acoustic phonons, the upper limit for the scattering rate of polar-optical phonons follows from

$$\lambda(E)=C'\int\int dK_x\,dK_y\frac{1}{(K_x^2+K_y^2)}\times\frac{\lambda(E)}{\eta^2(K_xK_y)+\lambda(E)}\,,\qquad C'=\left[\frac{e^2}{\gamma V\omega_0}\right]\left[\frac{A}{4\pi}\right]. \tag{14}$$

After some basic manipulation and a minor substitution, the integral may be written as

$$\lambda(E)=\frac{4C'}{\epsilon}\left[\frac{\pi^2}{D}\right]\int_{-\pi/2D}^{\pi/2D}\frac{dq_x}{q_x^2+(2\pi/4D)}\,,$$

which is

$$\lambda(E)=\frac{4C'}{\epsilon}\left[\frac{\pi^2}{D}\right]\frac{2D}{\pi}\left[\tan^{-1}\frac{Dq_x}{\pi}\right]\Bigg|_{-\pi/2D}^{\pi/2D}.$$

Finally, the upper limit is

$$\lambda_m = 5.48 \times 10^{13} \tag{15}$$

in units of $\sec^{-1}$.

## IV. FINAL-STATE SELECTION

The final process that must be evaluated before the Monte Carlo technique is complete is the determination of the final state after a scattering process. This final state depends on the type of process involved in scattering the electron to its final state. For the purpose of this work, acoustic phonons transfer no energy to or from the electron so the initial energy is the final energy. However, the polar-optical phonons extract or induce a constant quantum of energy ($\hbar\omega_0$) through emission or absorption. The final wave-vector state is determined by the magnitude of the density of states and any wave-vector dependence attributed to the matrix element. This is interpreted as a probability for scattering to or from a particular wave-vector state. Again, it is computationally and conceptually easier to work with a uniformly distributed random number. The expression $P(r)dr = P(K)dK$, where $r$ is a uniformly distributed random number is once more applied with $K$ the final wave vector.

It is a consequence of the complexity of the problem that the integral

$$r = \int_0^{K_f} P(K)\, dK$$

can rarely be integrated in a straightforward manner. Thus a technique due to von Neumann, called the rejection method, is required to calculate such expressions. In the rejection method, a trial value $\bar{K}$ is computed from

$$\bar{K} = a + (b-a)R_1 , \tag{16}$$

where $(a,b)$ are the limits on $K$ and $R_1$ is a uniformly distributed random number. If the condition

$$P(\bar{K}) \geq cR_2 \tag{17}$$

is satisfied, the $\bar{K}$ value is accepted and used as a member of the $K$ population being generated; otherwise, the process is repeated with two new random numbers. $R_2$ is another uniformly distributed random number and $c$ is the maximum value $\sup P(\bar{K}=[a,b])$.

The problem now becomes one of estimating a probability distribution for the phonon mechanisms. Since the acoustic phonons are completely randomizing so that all $\vec{K}$ vectors are equally likely. Thus the final $K$ state is determined by the density of states on the particular energy shell. For convenience, the field is taken in the direction of one of the major basis vectors of the two-dimensional LSSL. Therefore, the probability of being scattered is proportional to a one-dimensional density around the equal-energy contour. The corresponding probability for the final state of a scattering due to acoustic phonons is

$$P(K) \propto \left[ \frac{1-[B'-\cos(KD)]}{1-[B'-\cos(KD)]^2+\sin^2(KD)} \right]^{1/2} , \tag{18}$$

where $K$ is the magnitude of the final wave vector, and $B' = (\epsilon - E_K)/\epsilon$. A third random number is finally necessary to estimate the quadrant of the wave vector. These finally specify the scattering angle.

The final-state probability distribution for scattering due to polar-optical phonons follows a similar approach, but now a wave-vector contribution from the matrix element must be considered. The probability can accordingly be written as

$$P(K) = \frac{1}{|\vec{K}-\vec{K}'|^2} \times \left[ 1 + \frac{\sin^2(KD)}{1+[A+\cos(KD)]^2} \right]^{-1/2} , \tag{19}$$

which has the equivalent form

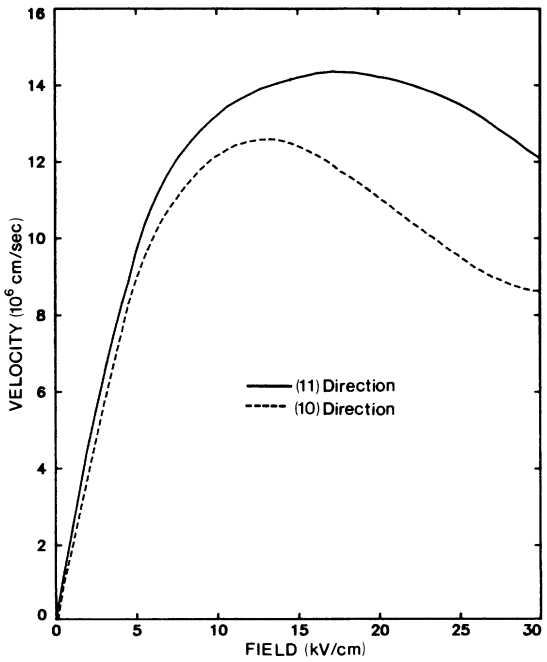


FIG. 5. Velocity vs field for the LSSL. At fields above 13 kV/cm the curves show a negative differential mobility region.

$$P(K)=\frac{1}{((K-K_x')^2+\{(1/D)\cos^{-1}[A-\cos(KD)]\}-K_y')^2}\left[\frac{1-[A-\cos(KD)]}{1-[A-\cos(KD)]^2+\sin^2(KD)}\right]^{1/2}. \quad (20)$$

Both $K_x', K_y'$ represent the initial-state wave vector from which the electron has been scattered. The calculation of the probability may be divided into regions, corresponding to regions of the energy contour to enable faster computation.

## V. RESULTS

In this section, all the work of the previous sections come together to develop the results obtained from the Monte Carlo simulation. These build the general framework for understanding the basic transport in the LSSL. The physics of the simulation is an ensemble that evolves in time and that can be used for transient calculations. A single band, sinusoidal in both dimensions of the LSSL, is considered. The third dimension is neglected because of its widely spaced discrete-energy levels. The lowest subband is totally filled, and therefore ignored, while the second is only partially filled and contains the electrons undergoing transport. Transitions to higher bands are insignificant and therefore ignored in their contribution to transport. The temperature of the lattice is assumed to be 300 K. Acoustic and polar-optical phonons are considered as the scattering processes. There is no inclusion of carrier-carrier scattering nor any type of breakdown mechanism at high fields. The relaxation times are as general as the Born approximation and are functions of energy. The electrons are accelerated by an applied static electric field whose direction is variable within the LSSL.

The transport properties are most easily observed with the velocity-field curve shown in Fig. 5. The lower curve results for a field applied along the (10) basis vector of the square-lattice array of cylinders (Fig. 1), while the top curve results for the field applied along the (11) direction. The low-field mobility for the (10) direction, which can be calculated using linear-response theory, is estimated to be about $\mu_0=1800$ cm$^2$/V sec. Likewise, the low-field mobility for the (11) curve is slightly larger than the (10) curve, and is $\mu_0=1900$ cm$^2$/V sec. This difference in value for the two directions is explained by the asymmetry of the conduction mass. The energy width in the (11) direction is larger in magnitude (by $\sqrt{2}$) than the (10) direction, and this energy width is responsible for the overall larger magnitude of the velocity at each field point in the (11) direction than in the (10) direction.

As the field is increased to approximately 10 kV/cm, the curves begin to show sublinear behavior and eventually peak near 13 kV/cm. For further increases in the field, the velocity actually decreases. For this model, the velocity continues to decrease to zero as the field tends to infinity.

The negative differential mobility, as well as the difference in peak velocity observed in the graph, is due to Bloch oscillations, where the electrons are able to cycle through the reduced Brillouin zone many times before they are scattered. Evidence for Bloch oscillations being the cause for the velocity decrease as a function of the field is seen in the curves for the fraction of electrons undergoing Bloch oscillation, in Fig. 6. (What is meant by fraction is the number of electrons actually undergoing Bloch oscillations divided by the total number of electrons.) Note that the field at which the velocity peaks and begins to decrease is related to that for approximately 50% reflection. A significant number of electrons are therefore freely cycling through the narrow bands.

The mean energy of the carrier ensemble may be extracted from the Monte Carlo simulation. This is shown in Fig. 7. The mean energy begins at the equilibrium value in the absence of an electric field. As the field is increased, the energy rises and, for all

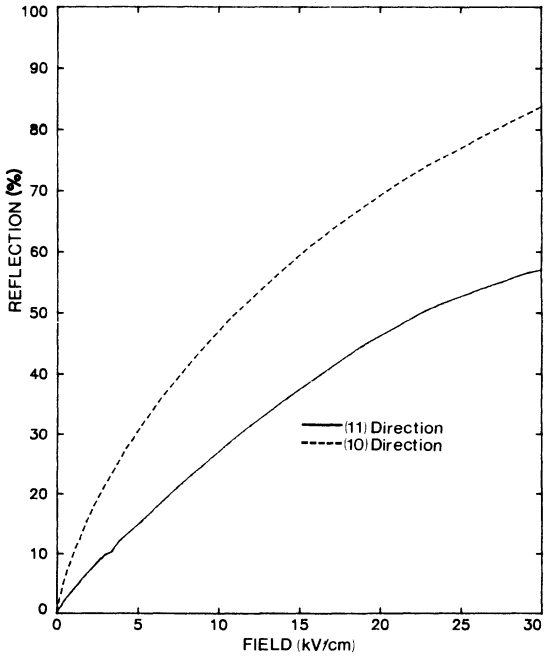


FIG. 6. Number of electrons that are not scattered before a traverse through the reduced Brillouin zone, normalized by total number of electrons.

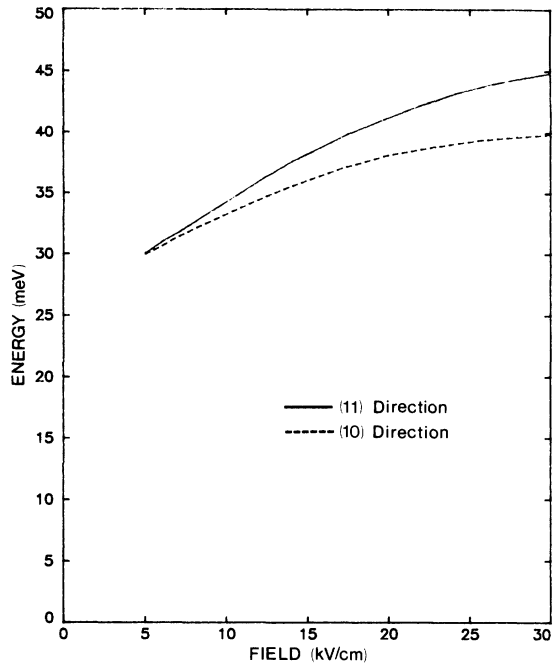


FIG. 7. Energy vs field for LSSL, displaying a saturation of energy at high fields.

practical purposes, saturates. The point at which the energy saturates corresponds to the point where the velocity also is near its peak. The saturation value of the mean energy is the half-filled-band energy. The (11) direction has a half-filled-band energy greater than that for the (10) direction and this explains the difference in energy saturation of the two curves.

Another indication for the existence of Bloch oscillations is found in the velocity-autocorrelation function. The numerical formula used in the calculation of the autocorrelation function is

$$\phi(\Delta t)=\frac{1}{N}\sum_{i=1}^{N} v_i(t)v_i(t+\Delta t)\ , \tag{21}$$

where $N$ is the number of particles and the sum is over all particles. The result of using this formula in the Monte Carlo simulation is shown in Fig. 8.

At low fields the autocorrelation function corresponds to that found for most homogeneous semiconductors, as observed for the curve of 12 kV/cm in Fig. 8. However, at higher fields the curves show peaks at long times that can be interpreted as the period for one, two, etc., cycles through the reduced Brillouin zone. As the field is further increased, the peaks are shifted closer together. This is associated with the higher acceleration, which in turn causes a shorter cycle time through the zone. Thus the Bloch oscillations are again substantiated by the velocity-autocorrelation function.

Lastly, the distribution function in momentum space for various fields has been calculated. At low

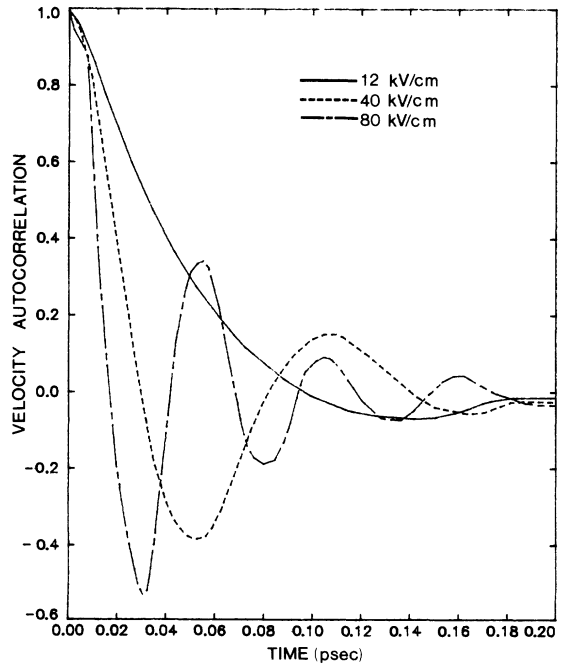


FIG. 8. Velocity-autocorrelation function vs time. At higher fields, oscillations in the correlation function occur at times corresponding to multiples of Bloch oscillator period.

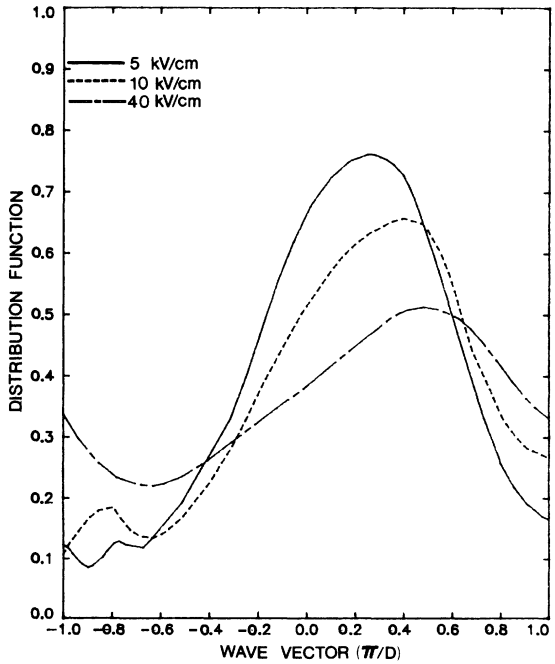


FIG. 9. Distribution function in $K$ space. The spacing between potential maxima are at $D=100$ Å. At high field, the distribution function tends to symmetric form.

fields, as for the 5-kV/cm curve in Fig. 9, the distribution function looks similar to a Gaussian, shifted by the electric field in the direction of the drift velocity. When the field is increased, the peak of the Gaussian decreases and the distribution begins to redistribute itself equally throughout $K$ space. The 10-kV/cm curve shows a shift in the peak to higher wave vector compared to the 5-kV/cm curve, but the peak has also decreased in magnitude. As the field is increased past that corresponding to the peak velocity, the antisymmetric distribution tends toward a symmetric distribution. The drift velocity which depends on the antisymmetric nature of the distribution of electrons in $K$ space thereby decreases. The dependence on the antisymmetric distribution is observed from

$$v_d = \int v_e(\vec{K}) f(\vec{K}) dV_K \ , \tag{22}$$

where $v_d(\vec{K})$ is the velocity for an electron and is antisymmetric. Therefore, the only contributions to the drift velocity will occur from the antisymmetric part of $f(\vec{K})$.

## VI. SUMMARY

The important aspects of the Monte Carlo simulation are contained in the negative differential mobility (NDM). All the results in this paper lend evidence to the presence of NDM in the velocity-field curves. The saturation in mean energy found from the Monte Carlo simulation provides a firmer foundation for this phenomena.

The distribution function pictured above does much to solidify the concept of Bloch oscillations in the LSSL. At low fields, the distribution is a displaced Maxwellian, as in an equivalent homogeneous semiconductor. However, as the field is increased, the electrons eventually redistribute themselves evenly throughout the band, as expected if the electrons are actually able to cycle through the reduced Brillouin zone. The $K$-space distribution function is symmetric at zero electric field, but becomes antisymmetric as the electric field is increased in the low-field region. However, the continuing increase of the field results in the reversion of the distribution function once again to a symmetric form. The cause of the functional dependence of the distribution on the electric field is associated with Bloch oscillations. The velocity-autocorrelation function displays definite oscillation peaks periodically placed in time. The period of the peaks is at approximately $2\pi\hbar/DeF$ (the time taken to cycle once through the reduced zone), thus again alluding to the physical cause for such behavior.

The NDM region is important in the respect that oscillations and large- and small-signal amplification can occur if such a region is present. An extensive amount of literature exists on velocity-field curves with similar shape to that exhibited here.[20–23] The commonly called Gunn-Hilsum effect[24,25] is one of the more notable phenomena reproducing this velocity-field curve. Much of the circuit analysis carried out for the Gunn-Hilsum effect applies also to the performance to the LSSL. Although the physical processes causing the NDM are widely different, it is the velocity-field curve that is required in most of the circuit operation. Since the velocity-field curves are similar, the circuit operation will therefore be similar. It should be remembered though, that because the physical causes of the NDM are different there will be modifications to some device performance.

## ACKNOWLEDGMENTS

The authors would like to thank Dr. G. J. Iafrate, United States Army Electronics Technology and Devices Laboratory, Ft. Monmouth, New Jersey, for helpful discussions. This work was supported by the U. S. Army Research Office.

[1]H. Kroemer, Phys. Rev. 109, 1856 (1958).
[2]R. E. Peierls, *Quantum Theory of Solids* (Oxford University Press, Oxford, 1955), p. 108.
[3]F. J. Ohkawa, Phys. Rev. B 24, 7297 (1981).
[4]P. J. Stiles, T. Cole, and A. A. Lakhani, J. Vac. Sci. Technol. 14, 969 (1966).
[5]A. B. Fowler, F. F. Fang, W. E. Howard, and P. J. Stiles, Phys. Rev. Lett. 16, 901 (1966).
[6]L. Esaki and R. Tsu, IBM J. Res. Dev. 14, 61 (1970).
[7]G. Abstreiter, G. H. Döhler, H. Künzel, D. Olego, K. Ploog, P. Ruden, and H. J. Stolz, Surf. Sci. 113, 479 (1982).
[8]H. Kroemer, Phys. Rev. B 15, 880 (1977).
[9]R. F. Kazarinov and R. A. Suris, Fiz. Tekh. Polyprovodn. 6, 148 (1972) [Sov. Phys.—Semicond. 6, 120 (1972)].
[10]R. T. Bate, Bull. Am. Phys. Soc. 22, 407 (1977).
[11]S. M. Sze, *Physics of Semiconductor Devices* (Wiley, New York, 1969), p. 20.
[12]G. J. Iafrate, D. K. Ferry, and R. K. Reich, Surf. Sci. 113, 485 (1982).
[13]N. Holonyak, Jr., W. D. Laidig, B. A. Vojak, K. Hess, J. J. Coleman, P. D. Dapkus, and J. Bardeen, Phys. Rev. Lett. 45, 1703 (1980).
[14]R. K. Reich and D. K. Ferry, Phys. Lett. 91A, 31 (1982).
[15]J. M. Ziman, *Electrons and Phonons* (Oxford University Press, Oxford, 1963), p. 47.
[16]H. D. Rees, J. Phys. Chem. Solids 30, 643 (1969).
[17]L. T. Schiff, *Quantum Mechanics*, 2nd ed. (McGraw-

Hill, New York, 1955).
[18]G. D. Mahan, *Many-Particle Physics* (Plenum, New York, 1981), Chap. 2.
[19]J. Stoer and R. Bulirsch, *Introduction to Numerical Analysis* (Springer, New York, 1980), Chap. 3.
[20]B. K. Ridley, J. Appl. Phys. 48, 754 (1974).
[21]H. L. Grubin, M. P. Shaw, and P. R. Solomon, IEEE Trans. Elec. Dev. ED-20, 63 (1973).
[22]J. B. Blott and W. Fawcett, *Advances in Microwaves,* edited by L. Young (Academic, New York, 1967), p. 223.
[23]D. E. McCumber and A. G. Chynoweth, IEEE Trans. Elec. Dev. ED-13, 4 (1966).
[24]J. B. Gunn, IBM J. Res. Dev. 8, 141 (1964).
[25]C. Hilsum, *Proceedings of the 7th International Conference on the Physics of Semiconductors, Paris, 1964,* edited by M. Hulin (Dunod Cie, Paris, 1964), p. 1127.